applied optics

Polarization holography for vortex retarders recording: laboratory demonstration

Pierre Piron,[1,*] Pascal Blain,[1] Marc Décultot,[1] Dimitri Mawet,[2] and Serge Habraken[1]

[1]Hololab, University of Liège, 17 Allée du 6 Août, 4000 Liège, Belgium
[2]Astronomy Department, California Institute of Technology, 1200 E. California Blvd., Pasadena California 91125, USA
*Corresponding author: pierre.piron@ulg.ac.be

Received 20 February 2015; revised 22 April 2015; accepted 22 April 2015; posted 23 April 2015 (Doc. ID 235018); published 15 May 2015

This paper will present a prototype of the first set of vortex retarders made of liquid crystal polymers recorded by polarization holography. Vortex retarders are birefringent plates characterized by a rotation of their fast axis. Liquid crystals possess birefringent properties and they are locally orientable. Their orientation is defined by the perpendicular to the local orientation of the recording field. Polarization holography is a purely optical recording method. It is based on the superimposition of coherent and differently polarized beams. It is used to shape the electric field pattern to enable the recording of vortex retarders. The paper details the mathematical model of the superimposition process. The recording setup is exposed; it is characterized by a nearly common path interferometer. Two sets of measurements allowing the prediction of the retarder's features are presented and compared. Finally, the experimentally recorded retarder is shown, its characteristics are investigated and compared to the predicted ones.

OCIS codes: (090.0090) Holography; (090.2880) Holographic interferometry; (260.5430) Polarization; (160.3710) Liquid crystals.

http://dx.doi.org/10.1364/AO.54.004765

1. INTRODUCTION

In a previous paper [1], we numerically demonstrated the possibility of recording vortex retarders (VRs) made of liquid crystal polymers (LCPs) using polarization holography to avoid mechanical action. This paper will present the first set of successfully recorded prototypes.

As a reminder, VRs are birefringent elements characterized by a uniform phase retard and a rotation of their fast axis along their center [see Fig. 1(b)]. After such a component, the transmitted beam is characterized by a phase dislocation following $\exp(il\theta)$ where θ is the azimuthal angle and l is the topological charge [2–5]. These particular retarders lead to several applications, such as coronagraphy [3,6–8], optical tweezing [9,10], plasmonic excitation with a focused beam [10,11], focusing into a spot smaller than the one obtained with a linearly polarized beam [10,12,13], etc.

Our retarders are composed of liquid crystals (LCs) which are aligned to form the desired fast axis rotation. The recording process consists of two steps [1,14]:

- An alignment layer, containing photosensitive polymers, is spin coated on a glass substrate. Then it is exposed to a linearly polarized UV beam and the polymers will align according to the perpendicular of the incident polarization.
- The LCPs layer is spin coated on top of the first layer and the LCs align themselves according to the polymers below. The second spin coating characteristics are chosen to reach a thickness achieving the half-wave condition near 660 nm: $\delta\phi = (2\pi\delta n h/\lambda_0) = \pi$, where δn is the birefringence. Afterward, it is exposed to UV source to fix the LCs in a frozen configuration.

Polarization holography is used to align the polymers of the first layer while avoiding mechanical action. The advantages of this method compared to others are the absence of contact for the LCs alignment and the possible absence or decrease of LCs misorientation areas near the rotation centers [15–17], which reduce the performances of the component. In a nutshell, polarization holography is the superimposition of differently polarized beams. It is used to achieve a specific polarization pattern inside the superimposition area.

In this paper, Section 2 briefly presents polarization holography with four beams. Section 3 details the recording setup. Section 4 investigates the prediction of the fast axis orientation in the retarder using two different sets of measurements. Then Section 5 presents the retarder, analyzes it, and compares it to the predictions. Finally, we resume our main achievements and present the future of this experimental research.

2. POLARIZATION HOLOGRAPHY WITH FOUR BEAMS

As stated before, polarization holography is used to shape the polarization pattern required to align the LCs to form VRs. To

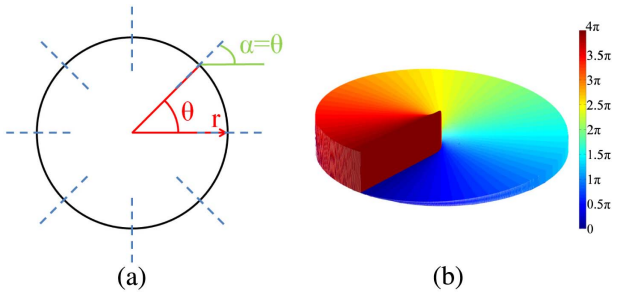

Fig. 1. Representation of a vortex retarder (VR) and the phase of the transmitted beam for the case of $l = 2$. (a) Represents the variation of the fast axis, in dashed blue lines, it rotates along the center for a total rotation of 2π. (b) Represents the phase distribution of a beam transmitted by the VR.

describe the local polarization ellipse, we used the same formalism as Kilosanidze and Kakauridze [18]. To create a rotational pattern, we chose a four-beams configuration. The four beams are represented by

$$A = \begin{pmatrix} A_x \\ A_y \exp(i\phi_A) \end{pmatrix} \exp(i\delta_A),$$
$$B = \begin{pmatrix} B_x \\ B_y \exp(i\phi_B) \end{pmatrix} \exp(i\delta_B),$$
$$C = \begin{pmatrix} C_x \\ C_y \exp(i\phi_C) \end{pmatrix} \exp(i\delta_C),$$
$$D = \begin{pmatrix} D_x \\ D_y \exp(i\phi_D) \end{pmatrix} \exp(i\delta_D). \quad (1)$$

To describe the local polarization ellipse, three parameters are used: I_1, I_2 are the intensities along the largest and smallest axes and θ is the orientation of the fast axis (see Fig. 2). They are computed using the following system of equations:

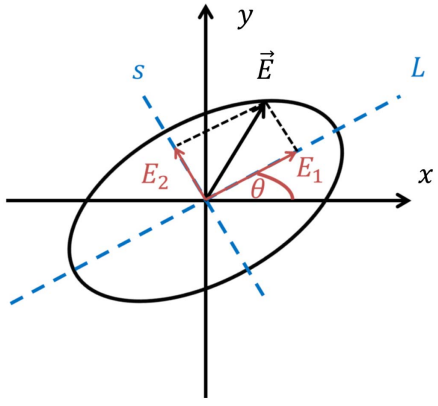

Fig. 2. Schematic representation of the local polarization ellipse. The largest axis (L) and the smallest axis (s) are pictured in dashed blue.

$$I_{1,2} = \frac{1}{2}[(p_x^2 + p_y^2) + (q_x^2 + q_y^2)] \pm \frac{1}{2}\sqrt{[(p_x^2 - p_y^2) + (q_x^2 - q_y^2)]^2 + 4(p_x p_y + q_x q_y)^2}$$
$$\sin(2\theta) = \frac{2(p_x p_y + q_x q_y)}{\sqrt{[(p_x^2 - p_y^2) + (q_x^2 - q_y^2)]^2 + 4(p_x p_y + q_x q_y)^2}}$$
$$\cos(2\theta) = \frac{(p_x^2 - p_y^2) + (q_x^2 - q_y^2)}{\sqrt{[(p_x^2 - p_y^2) + (q_x^2 - q_y^2)]^2 + 4(p_x p_y + q_x q_y)^2}}, \quad (2)$$

where $\mathbf{p} = \begin{pmatrix} p_x \\ p_y \end{pmatrix} = \Re(A + B + C + D)$ and $\mathbf{q} = \begin{pmatrix} q_x \\ q_y \end{pmatrix} = -\Im(A + B + C + D)$.

3. RECORDING SETUP

To create the four beams, we chose to use two Savart plates [19] with perpendicular directions of separation. The experimental setup is presented in Fig. 3 and the position and polarization state of the beams are pictured in Fig. 4.

The advantages of the recording setup with Savart plates is the compactness and robustness of the setup to vibrations due to the almost common path of the four beams.

In the next section, the orientation of the fast axis of the retarder will be predicted using two different sets of measurements.

4. PREDICTION OF THE RETARDER CHARACTERISTICS

As said in Section 1, the orientation of the fast axis in the final retarder is defined by the orientation of the recording electric field. To compute the orientation of the electric field, two sets of measurements can be used:

- the characteristics of the four superimposed beams,
- the Stokes parameters of the recording field.

A. Prediction Using the Beams Characteristics

The resulting electric field depends on the following parameters: σ the standard deviation of the Gaussian amplitude profile, d the distance between the four centers of the Gaussians (see Fig. 4), δ_i the phase retard of the incident beams compared to a beam B (see Fig. 4), I_i the relative intensities of the four beams, and α_i the orientation of the linear polarization of the four beams.

To measure σ, only the beam expander was mounted on the optical setup. Therefore, the intensity of the naked expanded beam was recorded at the exposure plane $\mathcal{E}$ in Fig. 3. Then the intensity was fitted with Matlab as a square Gaussian profile.

To compute δ_i, the beams were considered as plane waves with an incident angle θ_{in} at the exposing plane $\mathcal{E}$ in Fig. 3. To measure θ_{in}, the second Savart plate was briefly removed and a linear polarizer was added. That way, the intensity resulting from the superimposition of the two beams obtained at $\mathcal{D}$, was recorded at the exposing plane $\mathcal{E}$. The intensity pattern was a succession of horizontal fringes corresponding to the superimposition of two differently polarized beams [1,20].

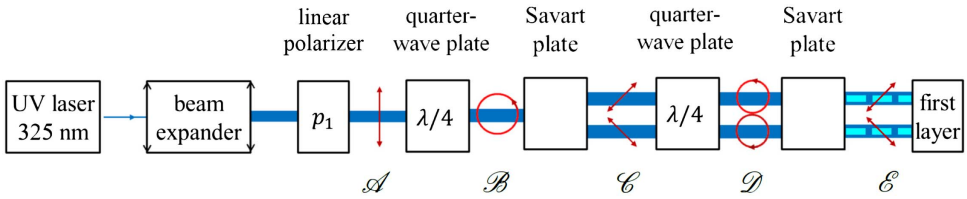

Fig. 3. Representation of the optical setup, the beams are pictured in blue and their polarization state in red. The first Savart plate possesses a vertical direction of separation while the second Savart plate possesses a horizontal one leading to the creation of four beams. Since the beams are circularly polarized before the Savart plates, the intensities of the transmitted beams are the same. Experimentally, the beams are wider and superimposed from $\mathcal{C}$ until the recording plane.

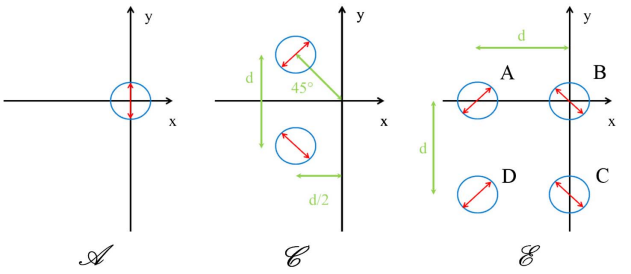

Fig. 4. Representation of the beams through the optical setup, the beams are pictured by blue circles and their polarization state by red arrows and d is the distance between the beams after the Savart plate. Experimentally, the beams are larger and they are superimposed at the different planes.

The distance between two consecutive fringes d_f was measured and θ_{in} was computed as $\theta_{\text{in}} = \arcsin(\lambda_{r0}/2d_f)$, where λ_{r0} is the recording wavelength in vacuum of 325 nm.

The other parameters (d, I_i, and α_i) were measured with the complete recording setup without the beam expander and a linear polarizer was added to measure α_i. The measured parameters are presented in Table 1.

The orientation of the local electric field was computed using these parameters with a more complex version of the code presented in Eqs. (1) and (2) including the Gaussian profile, the relative intensities, the polarization of the beams, etc. The results of this computation are presented in Fig. 5.

Table 1. Table of the Four Beams Characteristics Computed Thanks to the Different Measured Intensities[a]

Parameter	Lowest Value	Measured Value	Highest Value
$\sigma(mm)$	1.38	1.41	1.44
$\theta_{\text{in}}('')$	7.2	9	12
$d(mm)$	0.723	0.86	1
I_A	0.81	0.83	0.84
I_B	"1"	1	"1"
I_C	0.71	0.73	0.76
I_D	0.82	0.87	0.93
$\alpha_A = \alpha_D(°)$	43	45	47
$\alpha_B = \alpha_C(°)$	−47	−45	−43

[a]The lowest and highest values represent the extreme values of the parameters when the experimental error is taken into account.

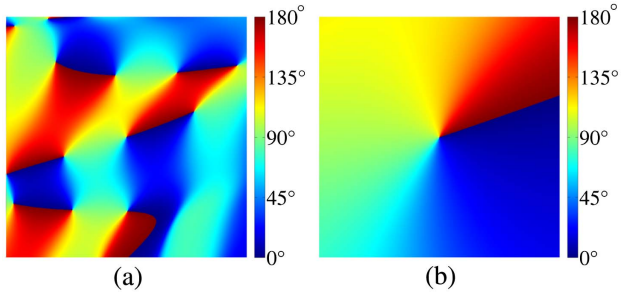

Fig. 5. Expected orientation variation of the electric field exposing the first layer obtained with the simulation based on the recording parameters; the computation domain is about 1.5 cm for (a) and 3 mm for (b). Several rotation centers can be observed and around a center, the fast axis rotates by 180°. The general orientation is pictured in (a) while (b) presents the orientation of the electric field around one rotation center.

Several features can be observed:

- The electric field rotates on himself about several points. These points will be defined as rotation centers.
- About a rotation center, the electric field rotates by 180°.
- The distance between two rotation centers (d_{c-c}) is 2.26 mm ± 44 μm.

Thanks to this local orientation, the fast axis of the future retarder can be computed. Using this fast axis pattern, one can compute the transmitted intensity of the retarder between two linear polarizers in a collimated beam. The phase retard $\Delta\phi$ of the simulated element is chosen as π. The justifications of this choice are listed below:

- to enhance the contrast,
- to stay close to the case of coronagraphic applications where half-wave plates are used [3,6–8],
- to be coherent with experimental reality.

This computed intensity is presented in Fig. 6.

B. Prediction Using the Stokes Parameters

To measure the Stokes parameters of the recording field, a linear polarizer was added at the end of the recording setup and the transmitted intensities were measured for different orientations of the polarizer. By solving the following system, one can compute the orientation of the local electric field θ [18,21]:

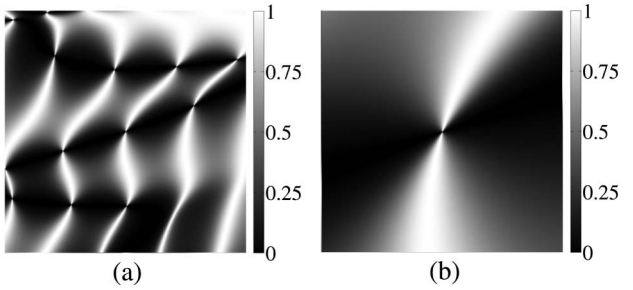

Fig. 6. Prediction of the transmitted intensity pattern for the expected half-wave plate between two crossed linear polarizers based on the four beams characteristics (half-wave plate recorded by the field pictured in Fig. 5). The beam is collimated and it is characterized by a uniform intensity set to one. The computing domain is about 1.5 cm for (a) and 2 mm for (b). The global intensity pattern is pictured in (a) while (b) represents the intensity around one rotation center. Around a rotation center, the intensity pattern presents two bright and two dark areas, which is the characteristic of $l = 1$ vortex retarders.

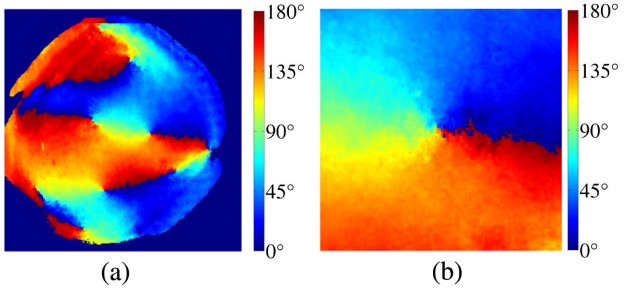

Fig. 7. Experimental orientation of the electric field at the first layer plane, obtained thanks to the measurement of the Stokes parameters; the computation domain is about 1 cm for (a) and 2 mm for (b). Several rotation centers can be observed and around a center, the fast axis rotates by 180°. The general orientation is pictured in (a) while (b) presents the orientation of the electric around one rotation center.

$$
\begin{aligned}
S_0 &= I_1 + I_2 \\
S_1 &= (I_1 - I_2)\cos(2\theta) \\
S_2 &= (I_1 - I_2)\sin(2\theta) \\
|S_3| &= (S_0^2 - S_1^2 - S_2^2)^{0.5}.
\end{aligned} \tag{3}
$$

The orientation of the electric field and a zoom on one rotation center are presented in Fig. 7.

Once again, the same three statements can be made:

- Several rotation centers are present, they are aligned on several lines.
- About one center, the electric field rotates by 180°.
- $d_{c-c} = 2.10\ \text{mm} \pm 50\ \mu\text{m}$.

Like Fig. 6, the transmitted intensity of the expected retarder between two linear polarizers can be computed using the orientation of the electric field. The results of the simulation are presented in Fig. 8.

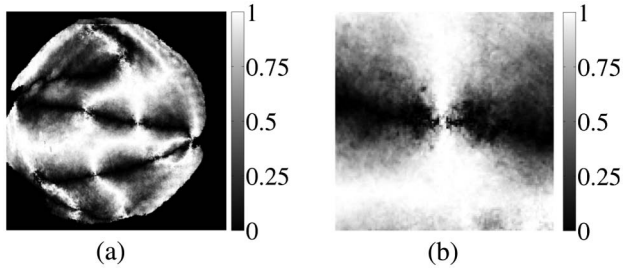

Fig. 8. Prediction of the transmitted intensity pattern for the expected half-wave plate between two crossed linear polarizers based on the Stokes parameters (half-wave plate recorded by the electric field pictured in Fig. 7). The beam is collimated and it is characterized by a uniform intensity set to one. The computing domain is about 1 cm for (a) and is about 2 mm for (b). The global intensity pattern is pictured in (a) while (b) represents the intensity around one rotation center. Around a rotation center, the intensity patter presents two bright and two dark areas, which is the characteristic of $l = 1$ vortex retarders.

C. Comparison between the Simulations

By comparing the results obtained in Subsections 4.A and 4.B, one can notice that the results are very similar: several rotation centers exist, the distance between two rotation centers is approximately the same, and the local electric field always rotates by 180°. However, the rotation centers pattern is different and the distance between the centers is not absolutely the same (≈5%). Several hypotheses can be made to explain the differences.

- The characteristics measured in Subsection 4.A were determined with a finite accuracy and an error between the real parameters and the measured one can exist.
- The mathematical model used in Subsection 4.A is a simple one. Indeed, the beams are considered as plane waves and the Savart plates are considered as perfect, while the experimental beams are spherical waves and the Savart plates may introduce aberrations such as astigmatism [22].
- During the rotation of the linear polarizer used in Subsection 4.B, a small translation of the beam is possible due to a non-normal incidence on the polarizer. This small translation may induce a change in the computed Stokes parameters and then change the computed orientation of the electric field.

D. Recording Limits

Another common point of the models is the drop of directionality near the rotation centers. Indeed, as the rotation center becomes close, the recording electric field grows more and more circularly polarized and at the rotation center, the beam is circularly polarized. Since the LCs orient themselves according to the perpendicular of the incident polarization, a local circularly polarized beam is unable to properly align them.

In a previous paper [14], we defined an eccentricity limit e where a more circularly polarized beam is unable to properly align the LCs. Experimentally, it corresponds to the polarization obtained after a linear polarizer and a quarter-wave plate with a fast axis forming an angle of 43° with the incident

polarization. Mathematically, it can be expressed as $e = \sqrt{1 - I_2/I_1} = 0.3611$.

Using this criterion, the misorientation areas were computed with the results presented in Subsections 4.A and 4.B and are presented in Figs. 9 and 10. It can be noticed that the maximum radius of the misorientation area is 87 μm ± 17 μm. It is about 5% of the distance between two rotation centers.

Thanks to previous experimental work [1,14], it could be determined that the minimal acceptable eccentricity was dependent of the collimation of the recording setup. Indeed, improving the collimation allows a less directional electric field to properly align the polymers of the first layer. It also increases the distance between two rotation centers. Therefore, it can be assumed that a better alignment of the beam expander and an improved collimated beam will reduce the percentage of the misorientation area.

In the next section, the recorded retarder will be presented.

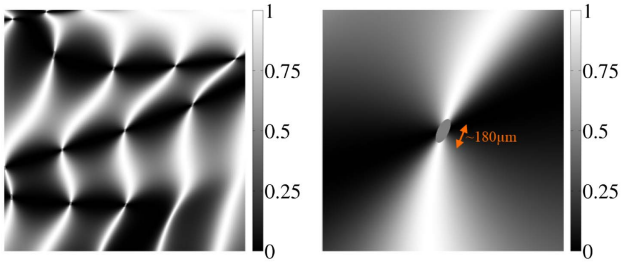

Fig. 9. Prediction of the transmitted intensity for the expected half-wave plate between two crossed linear polarizers with the misorientation areas based on the recording parameters. The misorientation areas are represented by a transmitted intensity of 0.5. The computing domain is about 1.5 cm for (a) and about 2 mm for (b). The global intensity pattern is pictured in (a) while (b) represents the intensity around one rotation center. The orange arrow in (b) represents the diameter of the misorientation area.

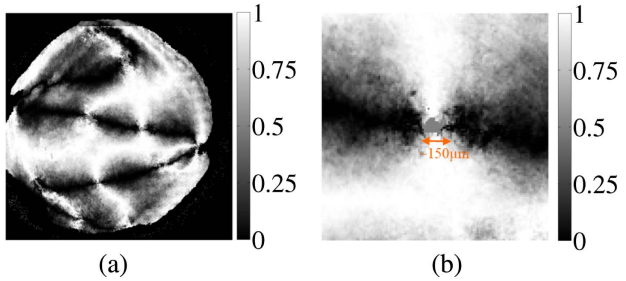

Fig. 10. Prediction of the transmitted intensity for the expected half-wave plate between two crossed linear polarizers with the misorientation areas based on the Stokes parameters. The misorientation areas are represented by a transmitted intensity of 0.5. The computing domain is about 1 cm for (a) and about 2 mm for (b). The global intensity pattern is pictured in (a) while (b) represents the intensity around one rotation center. The orange arrow in (b) represents the diameter of the misorientation area.

5. EXPERIMENTAL RESULTS

Finally, the retarder was recorded using the setup presented in Fig. 3. Since the second layer contains the birefringent molecules, its thickness will define the phase retard induced by the retarder. Due to our spin-coating process, the parameters defining the thickness of the layer are the rotation speed and the rotation time. We chose these parameters to reach a thickness of 2.3 μm corresponding to the half-wave condition near 660 nm ($\Delta\phi = \frac{2\pi\delta n h}{\lambda_0} = \pi$). The intensity of the recorded retarder between two linear polarizers obtained with a white source is presented in Fig. 11.

As it can be seen, the intensity pattern presents several rotation centers, the distance between two of them is 2.15 mm ± 0.1 mm. This distance is quite close to the expected ones (2.26 mm ± 0.04 mm for the first simulation and 2.10 mm ± 0.05 mm for the second one). Around a center, two bright and two dark areas are present meaning the fast axis rotates by 180° around it.

By comparing the transmitted intensities, it can be noticed that the intensity obtained thanks to the Stokes parameters is extremely close to the experimental one.

The difference between the predicted distance and the measured one is quite small ($\delta d_{c-c} \approx 10$ μm). Therefore we can conclude that the simulation using the measured Stokes parameters is the most accurate and the other simulation needs to be modified to achieve a mathematical model closer to experimental conditions.

Finally, to determine the misorientation of the LCs and to achieve a more accurate determination of the distance between two rotation centers, the retarder was placed between two crossed polarizers on a microscope and the transmitted intensity was recorded. Thanks to this measurement, the misorientation area of the LCs could be observed, its size could be measured as well as the distance between two rotation centers. The zoom on one rotation center is presented in Fig. 12.

Thanks to these measurements, the radius of the misorientation area and the distance between two rotation centers can be determined. The maximum radius of the misorientation areas is 89 μm ± 2 μm and the distance between two rotation centers is 2.16 mm ± 0.02 mm. Since the rotation centers pattern, the distance between two rotation centers and the radius of the misorientation area are close to the their experimental values for the prediction with the Stokes parameters, we can

Fig. 11. Transmitted intensities of the expected and recorded retarders between two crossed polarizers. (a) pictures the transmitted intensity computed thanks to the four beams features of Subsection 4.A, (b) depicts the transmitted intensity of the real retarder with a white source. Finally, (c) represents the transmitted intensity computed using the Stokes parameters of Subsection 4.B.

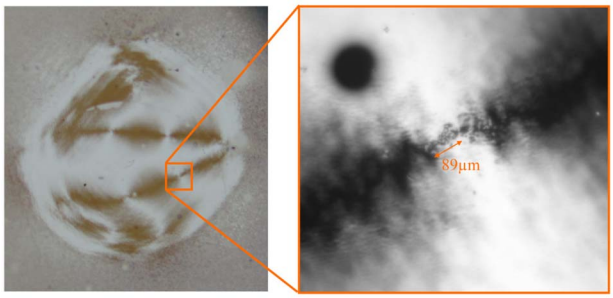

Fig. 12. General transmitted intensity (a) and zoom on one particular rotation center (b). On (b), the size of misorientation area corresponds to approximately 89 μm and the dark spot is a speck of dust on the LC layer.

conclude that the prediction with the Stokes parameters is effectively the best one.

6. CONCLUSIONS AND PERSPECTIVES

In this paper, the first series of VRs recorded with polarization holography was presented.

The mathematical model of polarization holography was developed for a four-beam superimposition. Then a purely optical recording setup was detailed. Afterward, two models to predict the local orientation of the recording field and the fast axis pattern of the recorded retarder were presented. The first one uses the polarization holography model with the four beams and their measured features; the second one uses the measurements of the Stokes parameters of the recording field. From these models, we claim that the retarders will possess several rotation centers and the fast axis of the retarder will rotate by 180° around the centers. Both models predict an area of misorientation of the LC due to the lack of directionality of the recording field.

Finally, the retarders are presented and compared to the models. The recorded retarders possess several rotation centers. Around each center, the fast axis rotates by 180° and the distance between the centers is comparable to the one expected from the two models. Also, near the rotation centers, the retarder presents a misorientation area of the LC with a radius of approximately 89 μm. It can be observed that the prediction using the Stokes parameters is better correlated to the experimental data.

Several improvements are ongoing. The first model based on polarization holography will be developed to include spherical wavefronts, imperfect collimation, and aberrations due to the Savart plates. The measurement process of the parameters could also be upgraded to achieve a higher accuracy on the parameters of the four beams and the Stokes parameters of the recording field. Moreover, by a better alignment of the beam expander, the collimation could be enhanced. A UV wavefront sensor will enable it. Consequently, the ellipticity limit will be smaller. Therefore, the distance between two rotation centers and the size of the misorientation area will be reduced. With this optimized setup, retarders containing only one rotation center could be recorded and analyzed to check their quality.

European Research Council (ERC) (337569); Fonds pour la formation à la Recherche dans l'Industrie et l'Agriculture (FRIA).

The authors want to thank Dr. Gene Serabyn and Dr. Kurt Liewer for their help with the measurement with a polarizing microscope of the phase retard induced by another prototype at the Jet Propulsion Laboratory.

The authors also wants to thank Loïc Lichawski and Julien Salon for their help during the manufacturing of the retarders.

REFERENCES

1. P. Piron, P. Blain, S. Habraken, and D. Mawet, "Polarization holography for vortex retarders recording," Appl. Opt. **52**, 7040–7048 (2013).
2. A. Niv, G. Biener, V. Kleiner, and E. Hasman, "Manipulation of the Pancharatnam phase in vectorial vortices," Opt. Express **14**, 4208–4220 (2006).
3. D. Mawet, E. Serabyn, K. Liewer, R. Buruss, J. Hickey, and D. Shemo, "The vector vortex coronagraph: laboratory results and first light at palomar observatory," Astrophys. J. **709**, 53–57 (2010).
4. M. Berry, "The adiabatic phase and Pancharatnam phase for polarized light," J. Mod. Opt. **34**, 1401–1407 (1987).
5. E. J. Galvez, "Applications of geometric phase in optics," in *Recent Research Developments in Optics 2* (Research Signpost, 2002), pp. 165–182.
6. D. Mawet, P. Riaud, O. Absil, and J. Surdej, "Annular groove phase mask coronagraph," Astrophys. J. **633**, 1191–1200 (2005).
7. D. Mawet, P. Riaud, J. Surdej, and J. Baudrand, "Subwavelength surface-relief gratings for stellar coronagraphy," Appl. Opt. **44**, 7313–7321 (2005).
8. C. Delacroix, O. Absil, P. Forsberg, D. Mawet, V. Christiaens, M. Karlsson, A. Boccaletti, P. Baudoz, M. Kuittinen, I. Vartiainen, J. Surdej, and S. Habraken, "Laboratory demonstration of a mid-infrared AGPM vector vortex coronagraph," Astron. Astrophys. **553**, A98 (2013).
9. Q. Zhan, "Trapping metallic Rayleigh particles with radial polarization," Opt. Express **12**, 3377–3382 (2004).
10. Q. Zhan, "Cylindrical vector beams: from mathematical concepts to applications," Adv. Opt. Photon. **1**, 1–57 (2009).
11. W. Chen, R. L. Nelson, D. C. Abesysinghe, and Q. Zhan, "Optimal plasmon focusing with spatial polarization engineering," Opt. Photon. News **20**, 36–41 (2009).
12. R. Dorn, S. Quabis, and G. Leuchs, "Sharper focus for a radially polarized light beam," Phys. Rev. Lett. **91**, 233901 (2003).
13. G. M. Lerman and U. Levy, "Effect of radial polarization and apodization on spot size under tight focusing conditions," Opt. Express **16**, 4567–4581 (2008).
14. P. Piron, P. Blain, M. Décultot, D. Mawet, and S. Habraken, "First prototypes of vortex retarders obtained by polarization holography," Proc. SPIE **9099**, 909911 (2014).
15. D. Mawet, E. Serabyn, K. Liewer, C. Hanot, S. McEldowney, D. Shemo, and N. O'Brien, "Optical vectorial vortex coronagraphs using liquid crystal polymers theory, manufacturing and laboratory demonstration," Opt. Express **17**, 1902–1918 (2009).
16. S.-W. Ko, C.-L. Ting, A. Y.-G. Fuh, and T.-H. Lin, "Polarization converters based on axially symmetric twisted nematic liquid crystal," Opt. Express **18**, 3601–3607 (2010).
17. S. R. Nersisyan, N. V. Tabiryan, D. Mawet, and E. Serabyn, "Improving vector vortex waveplates for high-contrast coronagraphy," Opt. Express **21**, 8205–8213 (2013).
18. B. Kilosanidze and G. Kakauridze, "Polarization-holographic gratings for analysis of light. 1. Analysis of completely polarized light," Appl. Opt. **46**, 1040–1049 (2007).
19. M. Françon and S. Mallick, *Polarization Interferometers: Applications in Microscopy and Macroscopy* (Wiley Intersciences, 1971).
20. P. Piron, P. Blain, and S. Habraken, "Polarization measurement with space-variant retarders in liquid crystal polymers," Proc. SPIE **8160**, 81600Q (2011).
21. B. Schaefer, E. Collet, R. Smyth, D. Barret, and B. Fraher, "Measuring the Stokes polarization parameters," Am. J. Phys **75**, 163–168 (2007).
22. M. C. Simon, "Image formation through monoaxial plane-parallel plates," Appl. Opt. **27**, 4176–4182 (1988).